Han *et al. Energy Mater* 2024;4:400001
DOI: 10.20517/energymater.2023.59

Energy Materials

Article

Open Access

Check for updates

Enhancing the long-term cycling stability of Ni-rich cathodes via regulating the length/width ratio of primary particle

Duzhao Han[1], Jilu Zhang[1], Mingyu Yang[1], Keyu Xie[2], Jiali Peng[3], Oleksandr Dolotko[3], Cheng Huang[4], Yuping Wu[5], Le Shao[6], Weibo Hua[1,*], Wei Tang[1,*]

[1]School of Chemical Engineering and Technology, Xi'an Jiaotong University, Xi'an 710049, Shaanxi, China.
[2]State Key Laboratory of Solidification Processing, School of Materials Science and Engineering, Northwestern Polytechnical University, Xi'an 710072, Shaanxi, China.
[3]Institute for Applied Materials (IAM), Karlsruhe Institute of Technology (KIT), Eggenstein-Leopoldshafen 76344, Germany.
[4]Guangdong Jiana Energy Technology Co., Ltd., Guangzhou 511449, Guangdong, China.
[5]School of Energy and Environment, Southeast University, Nanjing 210096, Jiangsu, China.
[6]Shaanxi Coal Chemical Industry Technology Research Institute Co., Ltd., Xi'an 710049, Shaanxi, China.

***Correspondence to:** Prof. Wei Tang, School of Chemical Engineering and Technology, Xi'an Jiaotong University, No. 28, West Xianning Road, Xi'an 710049, China. E-mail: tangw2018@xjtu.edu.cn; Prof. Weibo Hua, School of Chemical Engineering and Technology, Xi'an Jiaotong University, No. 28, West Xianning Road, Xi'an 710049, China. E-mail: weibo.hua@xjtu.edu.cn

How to cite this article: Han D, Zhang J, Yang M, Xie K, Peng J, Dolotko O, Huang C, Wu Y, Shao L, Hua W, Tang W. Enhancing the long-term cycling stability of Ni-rich cathodes via regulating the length/width ratio of primary particle. *Energy Mater* 2024;4:400001. https://dx.doi.org/10.20517/energymater.2023.59

Received: 10 Aug 2023 **First Decision:** 8 Oct 2023 **Revised:** 27 Oct 2023 **Accepted:** 29 Nov 2023 **Published:** 3 Jan 2024

Academic Editor: Meicheng Li **Copy Editor:** Fangling Lan **Production Editor:** Fangling Lan

Abstract

Ni-rich layered oxide cathode materials are promising candidates for high-specific-energy battery systems owing to their high reversible capacity. However, their widespread application is still severely impeded by severe capacity loss upon long-term cycling. It has been proven that the cyclic stability of Ni-rich cathode materials is closely related to their microstructure and morphology. Despite this, the influence of the microstructure of primary particles on the fatigue mechanism of Ni-rich cathode materials during prolonged cycling has not been fully understood. Here, two Ni-rich layered spherical agglomerate oxides consisting of the primary particle with different length/width ratios are successfully synthesized. It is found that the long-term structural stability of both materials strongly depends on the microstructure of primary crystallites, although there is no significant difference between the electrochemical and crystalline characteristics during the initial cycle. A higher primary particle length/width ratio could effectively inhibit the accumulation of microcracks and chemical degradation during long-term cycling, thereby promoting the electrochemical performance of the cathode materials (80% capacity retention after

200 cycles at 1 C compared to the 55% of the counterpart with a lower primary particle length/width ratio). This study highlights the structure-activity relationship between the primary particle microstructure and fatigue mechanisms during long-term cycling, thereby advancing the development of Ni-rich cathode materials.

Keywords: Ni-rich layered oxide, primary particle length/width ratio, long-term cycling, microcracks, cycling stability

INTRODUCTION

Lithium-ion batteries (LIBs) have gained wide popularity in renewable energy-related fields owing to their numerous advantages, including high energy density, cost-effectiveness, and safety[1]. Nevertheless, the immense demand for high-specific-energy LIBs necessitates further developments, especially in the areas of electric vehicles (EVs) and energy storage systems. The urgent need to explore high-capacity cathode materials has arisen since the energy density and cost of LIBs are chiefly limited by cathode materials[2]. Ni-rich layered oxides, such as $LiNi_xCo_yMn_zO_2$ (NCM, where $x + y + z = 1$ and $x \geq 0.8$) and $LiNi_xCo_yAl_zO_2$ (NCA), are viewed as potential cathode materials for the next-generation LIBs owing to their high discharge capacity (> 200 mAh g^{-1}), high working potential, and low manufacture cost[3,4]. However, the increased nickel content in NCM or NCA also poses severe chemical and structural instability issues upon long-term cycling, mainly originating from accumulations of the cathode-electrolyte interphase (CEI), electrolyte decomposition, formation of inactive rock-salt phase on the particle surface, and propagation of microcracks induced by the anisotropic unit cell volume expansion/contraction[5,6].

Tremendous endeavor has been devoted to enhancing the cycling stability of Ni-rich cathode materials, e.g., doping[7,8], surface coating[9,10], concentration gradients, and single-crystalline morphology[11]. Furthermore, considerable attention has been given to the physical/chemical features of primary particles (e.g., size, morphology, arrangement, *etc.*), as they significantly influence the electrochemical performance of cathode materials[12]. Consequently, numerous reports have emerged concerning microstructure texture, with the objective of mitigating structural degradation and enhancing the cycling stability of Ni-rich layered cathode materials. Introducing low-solubility dopants to refine primary particle size serves to dissipate the local internal strain caused by abrupt lattice collapse, thereby suppressing the propagation of microcracks and strengthening the mechanical integrity of cathode materials[13]. Moreover, the manipulation of target lattice facet orientation in primary particles, aiming to elevate the oxygen stability or improve ion transfer kinetics, represents an effective strategy in the engineering of Ni-rich cathodes[14]. While numerous reports have focused on element doping with surface energy modification (such as B, Mo, Nb, *etc.*) to tailor the primary particle, this approach often results in sacrificed available capacity and increased process cost[15-17]. In contrast, there has been limited research on regulating microstructure through adjusting processing conditions, which offers the unique advantage of inheriting the particle structure characteristics from the precursor to the final cathode materials. Furthermore, the interrelated mechanism between the cathode material primary particle length/width ratio and the capacity decay upon prolonged cycling remains unclear.

In this work, $[Ni_{0.8}Co_{0.1}Mn_{0.1}](OH)_2$ precursors and corresponding $Li[Ni_{0.8}Co_{0.1}Mn_{0.1}]O_2$ (NCM811) cathode materials with two distinct primary particle length/width ratios were synthesized by manipulating the co-precipitation synthetic conditions. The electrochemical performance properties, structural evolution, and fatigue mechanism of NCM811 were thoroughly investigated via *in situ* X-ray radiation diffraction (XRD), electrochemical tests, and post-mortem analysis. During the initial lithiation/delithiation process, both cathode materials exhibited similar discharge specific capacity and lattice parameter evolution. However, a

higher primary particle length/width ratio demonstrated an effective alleviation of the propagation of microcracks, thus mitigating accumulated surface chemical degradation and improving phase transition reversibility. This led to superior cycling stability and structural reversibility for the Ni-rich cathode with a higher primary particle length/width ratio (namely, HR-NCM), as evidenced by an impressive capacity retention of 80% after 200 cycles at 1 C. In contrast, the oxide with the lower length/width ratio (LR-NCM) exhibited a capacity retention of only 55%. This work sheds light on the relationship between primary particle length/width ratios and long-term cycling stability of Ni-rich cathode materials. These findings are significant in guiding the design of desired high-specific-energy LIBs.

EXPERIMENTAL

Synthesis of materials

The hydroxide precursors $[Ni_{0.8}Co_{0.1}Mn_{0.1}](OH)_2$ were synthesized via a co-precipitation method. Transition metal sulfates, including $NiSO_4·6H_2O$, $CoSO_4·7H_2O$, and $MnSO_4·H_2O$, in molar ratios of Ni/Co/Mn = 8:1:1 were slowly added into a continuously stirred tank reactor with $NH_3·H_2O$ as a chelating agent. To maintain the pH level, a 4 M NaOH (aq.) solution was simultaneously pumped into the reactor. The pH was controlled within the range of 10.95-11.05 for HR-precursor synthesis and 11.40-11.50 for LR-precursor synthesis. N_2 gas was continuously fed into the reactor to maintain an inert atmosphere during synthesis. The synthesized precursors were collected via vacuum filtration, washed with deionized water, and dried in an oven at 110 °C for 24 h. The as-synthesized precursors were then mixed thoroughly with a specific amount of $LiOH·H_2O$ with a molar ratio of 1:1.05 (the excess lithium was used to compensate for lithium loss during the calcination process), preheated at 500 °C for 6 h, and calcined at 780 °C for 12 h in a pure O_2 atmosphere to produce the $LiNi_{0.8}Co_{0.1}Mn_{0.1}O_2$ cathode materials.

Characterization

The chemical composition of synthesized oxide materials was analyzed using an inductively coupled plasma atomic emission spectrometer (ICP-AES, Agilent 7800). The crystal structure of the cathode powder samples was determined using *ex situ* high-resolution synchrotron-based XRD (sXRD) at beamline P02.1 with synchrotron radiation energy of 60 keV (λ = 0.2072 Å) at the DESY (Deutsches Elektronen synchrotron) in Hamburg, Germany. The crystal structure evolution of the cathodes during the initial charge-discharge process was analyzed using *in situ* XRD with Ag Kα radiation (Bruker D8 ADVANCE, λ = 0.5594 Å), and the crystallographic parameters were obtained using the Rietveld method and FullProf program. XRD with Cu Kα radiation (Bruker D8 ADVANCE, λ = 1.5406 Å) was used to characterize the crystal structures of precursors and cathode electrodes before and after cycling. The morphologies and microstructures of the precursors and cathode materials were observed using scanning electron microscopy (SEM, Zeiss Merlin), and cross-section SEM samples were prepared with a cross-section polisher (CP, IB-19510 JEOL). Transmission electron microscopy (TEM) and energy Dispersive Spectroscopy (EDS) mapping images were captured using JEOL JEM-2100 equipment operating at 200 keV. The surface chemistry of the electrodes was analyzed using X-ray photoelectron spectroscopy (XPS, Thermo Scientific K α spectrometer). Finally, all cycled electrode samples were rinsed with diethyl carbonate (DEC) solvents to remove residual electrolyte salts and by-products before the relevant characteristics were analyzed.

Electrochemical tests

To fabricate the cathode electrodes, a mixture of cathode material powders, super P, and poly(vinylidene fluoride) in a weight ratio of 80:10:10 was fully blended in N-methyl-2-pyrrolidone. The resulting slurry was applied onto aluminum foil and dried under vacuum at 60 °C for 24 h. Lithium metal cells were constructed using CR-2032 coin cells in an Ar-filled glovebox with the cathode and lithium metal foils serving as the counter and reference electrode, respectively. The electrolyte used was 1 M $LiPF_6$ in EC/DEC/DMC (1:1:1 Vol%) with 5 wt% FEC as an additive. The electrochemical cycling performance of the cells was tested

using battery-test equipment (Neware) between 2.7 and 4.3 V (*vs.* Li/Li^+) at 25 °C. To evaluate the rate capability, the cells underwent charging and discharging at rates ranging from 0.1 to 15 C. Electrochemical impedance spectroscopy (EIS) analysis was performed using a Princeton electrochemical workstation over a frequency range of 10 mHz to 100 kHz with an amplitude of 10 mV. Galvanostatic intermittent titration technique (GITT) measurements were carried out using current pulses (100 mA g^{-1}) with a duration of 10 min and a relaxation process of over 2 h. Cyclic voltammogram (CV) scans for the cells were recorded using a Princeton electrochemical workstation at a scanning rate of 0.1 mV s^{-1}.

RESULTS AND DISCUSSION

The hydroxide precursors with different primary particle sizes were obtained using a typical co-precipitation synthesis method, and details of the preparation process are in the Supporting Information. Supplementary Figure 1 illustrates that the XRD patterns of the obtained precursors were similar to the standard spectra of β-$Ni(OH)_2$ (PDF#14-0117). All diffraction reflections could be indexed to a hexagonal structure with a space group of *P-3m1*[18]. In addition to this, SEM analysis characterized the morphology of the synthesized precursors. The spherical-like morphology of the secondary particles in both precursors, composed of nanosheet primary particles, was evident in Supplementary Figure 2, Figure 1A and B. While the width of primary particles in the LR-precursor was noticeably larger than that in the HR-precursor, this difference can be attributed to the competition between nucleation and complexation under different co-precipitation pH conditions[13]. The growth process of hydroxide precursors can be divided into three main stages, including nucleation and growth of single crystalline grains, agglomeration to form primary particles, and the subsequent growth of secondary particles. The higher pH condition accelerates the nucleation process and promotes the formation of hydroxide crystal nuclei. These nuclei then agglomerate on the surface of as-formed primary particles, which finally construct thicker primary particles within the LR-precursor.

The precursors were further mixed with lithium sources to synthesize the Ni-rich layered oxides via high-temperature lithiation reactions. The composition of HR-NCM and LR-NCM was verified using ICP-AES, revealing that the Ni, Co, and Mn atom ratios aligned with the target compositions [Supplementary Table 1]. Figure 1C and D shows the XRD patterns of HR-NCM and LR-NCM cathodes and corresponding Rietveld refinement plots. All the diffraction peaks can be well indexed as hexagonal α-$NaFeO_2$ layered structures belonging to the *R-3m* space group without any extra reflections denoting an impurity phase[19]. Notably, the XRD patterns showed a clear splitting between 006/102 and 108/110 reflections, implying a well-ordered layered structure for both samples [Supplementary Figure 3]. Moreover, the integrated intensity ratio of I_{003}/I_{104} in the two oxides was greater than 1.2 [Supplementary Figure 4], indicating negligible cation mixing[20]. These results align with the degree of Li^+/Ni^{2+} mixing in the Li layer, as determined from the refinement results (i.e., 1.31% for HR-NCM and 1.34% for LR-NCM, Supplementary Tables 2 and 3). Furthermore, the elemental mappings depicted in Supplementary Figures 5 and 6 demonstrate the homogeneous distribution of Ni, Co, Mn, and O in both cathodes at the micrometer scale. Notably, the materials exhibit the formation of micro-sized secondary particles with tightly-packed nanosized primary particles, as illustrated by the inserted SEM images in Figure 1C and D. Furthermore, the size distribution of primary particles in Ni-rich layered oxides was obtained by measuring the length and width of single primary particles one by one in ImageJ software. The statistical analysis in Figure 1E and F reveals a higher average length/width ratio distribution of primary particles for HR-NCM (2.2) than for LR-NCM (1.7), which is highly related to the primary particle size characteristics in their precursor. As depicted in Figure 1G, a high-resolution TEM image of HR-NCM displays an average interplanar distance of approximately 0.47 nm, corresponding to the (003) crystal plane of the layered structure (*R-3m*)[21].

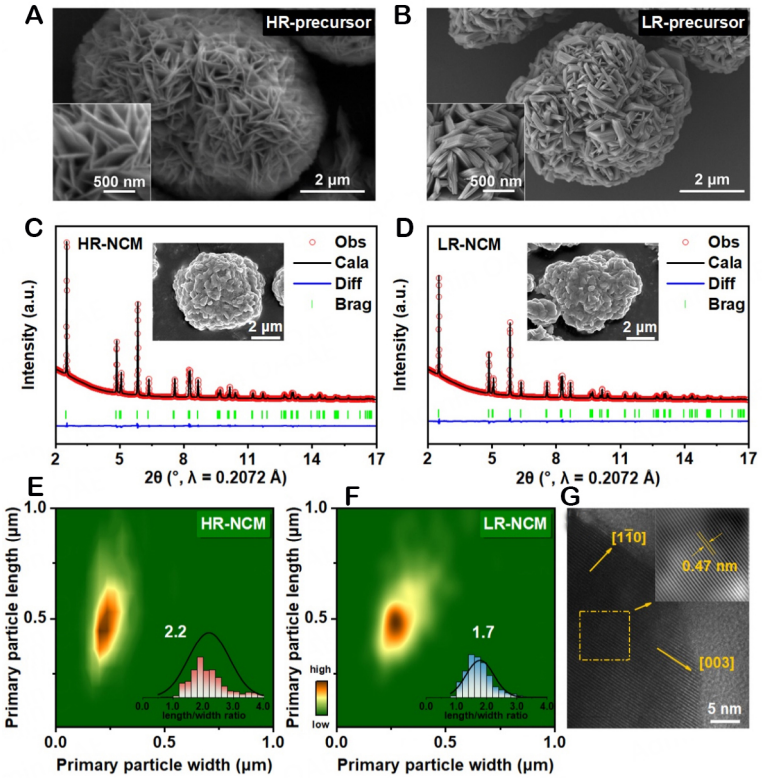

Figure 1. The SEM images of (A) HR-precursors and (B) LR-precursor particles (insert: the enlarged view). The sXRD Rietveld refinement patterns against (C) HR-NCM and (D) LR-NCM powder samples, the inserts are corresponding SEM images of HR-NCM and LR-NCM. The statistical diagram of primary particle sizes: (E) HR-NCM and (F) LR-NCM (insert: the statistical analysis of primary particle length/width ratio). (G) HR-TEM image of HR-NCM. The insert is the corresponding HRTEM image showing a lattice spacing of 0.47 nm for the layered (003) planes.

The electrochemical properties of the HR-NCM and LR-NCM cathodes were evaluated in CR2032-type half cells constructed using lithium metal as the anode. Figure 2A depicts the initial capacity-voltage curves of the HR-NCM and LR-NCM cathodes at a rate of 0.1 C (1 C = 200 mAh g^{-1}) from 2.7 to 4.3 V. The electrochemical curves are strikingly similar, and both cathodes exhibit a high and similar initial discharge specific capacity at 0.1 C, which is approximately 200 mAh g^{-1} (204.6 mAh g^{-1} for HR-NCM and 203.7 mAh g^{-1} for LR-NCM). The corresponding dQ dV^{-1} curves were obtained by differentiating the initial charge and discharge profiles [Supplementary Figure 7]. As the cathodes underwent lithiation/delithiation, they experienced a series of phase transitions associated with four distinct redox peaks (hexagonal (H1) → monoclinic (M) → hexagonal (H2) → hexagonal (H3) phase)[22]. CV tests were also conducted to examine the redox reactions and phase transitions that occur during the charge/discharge processes. Supplementary Figure 8 illustrates that both cathodes exhibit comparable redox behaviors consistent with the dQ dV^{-1} curves. The dissimilarity in anodic peaks during the initial cycle contributed to the formation of the CEI[23]. The electrochemical polarization and irreversible reaction correspond to the potential intervals (ΔV) between the H1↔M reduction/oxidation peaks. In the HR-NCM cathode, the ΔV is 0.09 V, which is smaller than that of the LR-NCM (0.16 V), indicating smaller polarization during the initial scanning for the HR-NCM.

Figure 2B illustrates the cycling stability of two cathodes at 1 C in the voltage range of 2.7-4.3 V. The HR-NCM cathode displays excellent capacity retention at 80% after 200 cycles, while the LR-NCM cathode experiences a rapid decrease in capacity, dropping to 55% over the same number of cycles. In addition, the

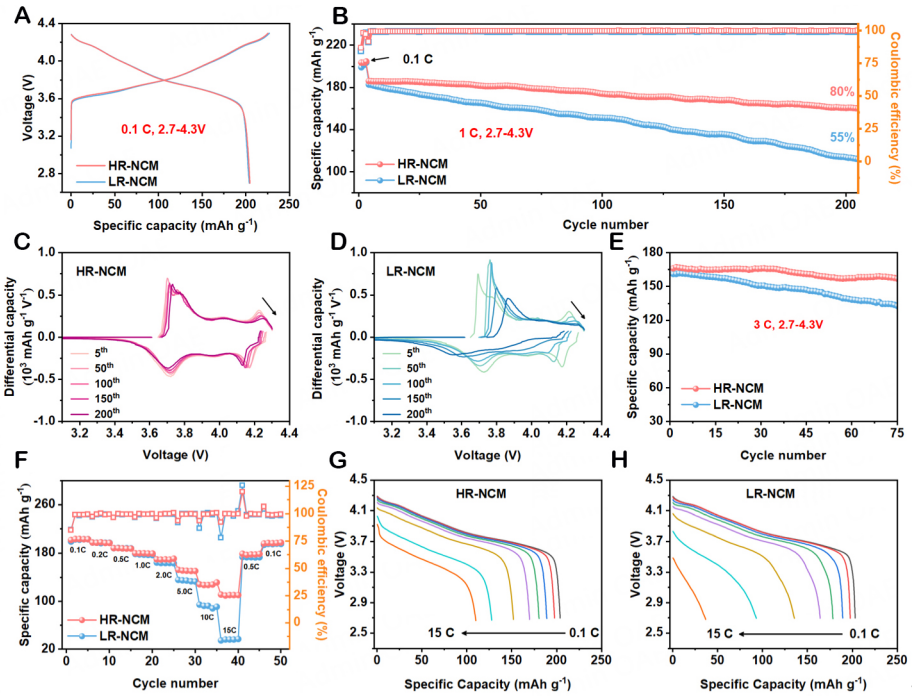

Figure 2. Electrochemical properties of the HR-NCM and LR-NCM cathodes in the voltage range of 2.7-4.3 V. (A) The initial charge/discharge voltage curves of both cathodes at 0.1 C. (B) Cycling performance and (C and D) the corresponding d*Q* d*V*$^{-1}$ curves at different cycles at 1 C. (E) Cycling performance at 3 C. (F) Rate capability of cathodes from 0.1 C to 15 C and the first discharge curves under various current densities of (G) HR-NCM and (H) LR-NCM cathodes.

HR-NCM cathode demonstrates outstanding voltage stability during cycling according to the charge-discharge curves from the 1st to the 200th cycles [Supplementary Figure 9]. Furthermore, after 200 cycles, the HR-NCM cathode exhibits a voltage decay of only 0.035 V, a significantly lower value than that of LR-NCM (0.232 V). To delve more into the effect of primary particle length/width ratios on the phase transitions and electrochemical polarization during long-term cycling for HR-NCM and LR-NCM, Figure 2C and D displays the calculated different capacity (d*Q* d*V*$^{-1}$) curves at various cycles. The H2 ↔ H3 redox peaks exhibit varying degrees of intensity fading and polarization upon prolonged cycling in both cathodes, providing evidence for the accumulation of the irreversible H3 phase and the degradation of the crystal structure. Nevertheless, HR-NCM displays superior stability in the intensity and polarization voltage of phase transition peaks compared to LR-NCM, highlighting its enhanced structural stability and consistency with its better capacity retention in Figure 2B[24,25]. Additionally, as illustrated in Figure 2E, the HR-NCM cathode also demonstrates relatively superior cycling stability even under higher charge/discharge rates of 3 C in the voltage range of 2.7-4.3 V.

The Li-ion transportation characteristics of two cathode materials were evaluated by testing rate performance at varying current densities from 0.1 C to 15 C [Figure 2F]. Both cathodes showed similar capacity at a relatively low rate of 0.1 C. However, as the applied current density increased, the LR-NCM cathode displayed severe capacity decay, while the HR-NCM exhibited excellent capacity retention. Even at 15 C, the HR-NCM retained a high discharge capacity of ~110 mAh g^{-1}, which is much superior to that of the LR-NCM (~37 mAh g^{-1}). The capacity-voltage curves of the HR-NCM were also well maintained at different rates compared to the LR-NCM cathode [Figure 2G and H]. To gain a better understanding of the Li^+ diffusion kinetics of the cathode materials, GITT measurements were conducted [Supplementary Figures 10 and 11]. The calculated Li^+ diffusion coefficients between 2.7 and 4.3 V for the

charge and discharge process, respectively, demonstrated that the HR-NCM cathode possessed higher Li^+ diffusion ability at various states of charge (SOC) and depths of discharge (DOD) than the LR-NCM[26,27]. In addition, the corresponding voltage-time curves were used to evaluate the electrochemical polarization for both cathode materials at a selected point of about 3.8 V at the charging platform [Supplementary Figure 11]. The HR-NCM electrode exhibited a lower voltage drop in the titration step and a higher diffusion coefficient than the LR-NCM electrode, indicating fast kinetics of the cathode with a higher primary particle length/width ratio. Furthermore, the apparent activation energy (E_a) for the Li-ion intercalation reaction of both cathodes was investigated to evaluate the interfacial transfer kinetics. As shown in Supplementary Figure 12, the value of E_a for HR-NCM (0.35 eV) is smaller than that of LR-NCM (0.44 eV), which is in good agreement with the diffusion coefficient obtained from the GITT tests. The aforementioned results suggest that the electrochemical process in the LR-NCM cathode is kinetically limited by slower Li^+ diffusion, which may be the origin of the poor rate performance of the LR-NCM.

The evolution of the structure and lattice parameters of NCM cathodes is not only dependent on the crystal structure properties of materials but also regulated by the microstructure texture of material particles. Thus, *in situ* XRD analysis was further performed on Li/HR-NCM and Li/LR-NCM cells during the initial cycle to conduct an accurate study on the structural evolution of the cathode materials with distinct primary particle length/width ratios during the electrochemical process. The *in situ* XRD patterns of both cathodes exhibited a similar evolution of reflection shift during cycling [Supplementary Figures 13 and 14]. Charge-discharge curves and contour maps of 003 and 110 reflection (representing the *c* and *a* lattice parameter, respectively) were presented in Figure 3A and B. For both cathodes, the 110 reflection gradually shifts towards higher angles during the charging process, indicating the monotonous decrease in the *a* lattice parameter due to the oxidation of transition metals and decreased ionic radius in the transition metal layers[14,28]. At a low delithiation state, the 003 reflection slightly shifts to a lower angle, indicating the expansion of the *c* lattice parameter owing to the intensified electrostatic repulsive force between neighboring oxygen slabs when the Li ions deintercalated from the Li layers[29]. Upon further charging, the 003 reflection markedly shifts to a higher angle owing to eliminated pillar effects along with the reduced electrostatic repulsion triggered by the increase of Ni^{4+}-O^{2-} covalent bonding strength[30], indicating the contraction of the unit cell along the *c*-axis. Furthermore, Figure 3C-E plots the change in *a*, *c*, and unit cell volume of the cathode materials as a function of the SOC during the charging process. The *a* lattice parameter varied by approximately 1.9% for both cathodes in the initial charge process. There is no discernible difference in the maximum *c* lattice parameter contraction between both cathodes (2.2% for HR-NCM and 2.1% for LR-NCM). These results suggest that the length/width ratio of the primary particles has no significant effect on the initial crystal structural evolution of the synthesized cathode materials. It is important to note that the evolution of lattice parameters during the charge/discharge process was highly anisotropic, which could potentially result in the generation and propagation of microcracks after prolonged cycling[31,32]. Therefore, more research is needed to understand the impact of primary particle length/width ratios on the structural stability of cathodes.

To investigate the accumulated structural deterioration in cathode materials upon long-term cycling, a series of post-mortem characterizations were carried out. Firstly, the structural stability of cathodes was evaluated by comparing the XRD patterns before and after 100 cycles [Figure 4A]. No significant changes were observed in the XRD patterns of fatigued HR-NCM and LR-NCM, and the extra reflections could be attributed to the Al current collector. Notably, as shown in Figure 4B and Supplementary Table 4, the 003 reflections for both cathodes slightly shifted to lower angles after cycling, indicating an increased lattice parameter *c*. However, the shift of the 003 reflection for HR-NCM (0.26°, corresponding to the increased *c* from 14.1930 Å to 14.2025 Å) was smaller than that of LR-NCM (0.31°, corresponding to the increased *c* from 14.2017 Å to 14.3132 Å). Moreover, the splitting of 006/102 reflections for HR-NCM was well retained

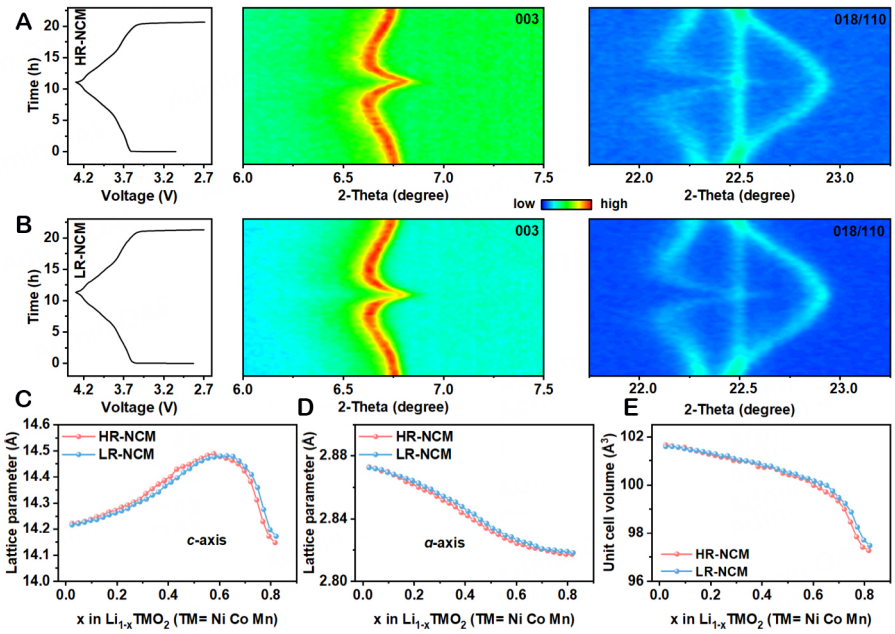

Figure 3. Contour plots of *in situ* XRD patterns of (A) HR-NCM and (B) LR-NCM for 003 and 018/110 reflections and the corresponding charge-discharge curves during the initial cycle. Lattice parameters of the (C) *c*-axis, (D) *a*-axis, and (E) unit cell volume as a function of the state of charge for both cathodes.

after 100 cycles, which differed from the nearly disappeared splitting reflection of LR-NCM [Supplementary Figure 15]. Therefore, the XRD patterns suggest that Ni-rich cathode materials with a higher primary particle length/width ratio possess better structural stability during long-term cycling[21,33]. Furthermore, cross-sectional SEM images of fatigued electrodes were examined in the discharge state to track the morphological changes [Figure 4C and D]. Compared to the fresh cathode materials [Supplementary Figure 16], microcracks were observed in the internal area of cathode material secondary particles after cycles due to the repeated anisotropic lattice parameter changes during Li-ion insertion/extraction processes. Extensive microcracks were observed in the secondary particle of fatigued LR-NCM electrodes [Figure 4D], while only a few microcracks were present in the cycled HR-NCM cathode [Figure 4C]. The presence of microcracks propagated to the outside surface of particles provides numerous channels for electrolyte penetration to the inner particles. This allows the electrolyte to react with the newly exposed active cathode substances and aggravates more parasitic reactions[34]. Such reactions generally induce extensive generation of an inactivated NiO-like rock-salt phase and a CEI layer with transition metal dissolution, resulting in capacity fading and structural collapse upon cycling[35]. Besides, the difference in the primary particle length/width ratios also reflects the relative exposure of crystal planes with varying chemical stability to resist the oxygen vacancy formation and side reactions with electrolytes, which influences the stability of the cathode materials[36].

To further investigate the evolution of the structure and chemistry of cathode material surfaces, XPS measurements of C 1s, O 1s, and F 1s spectra were first conducted on the electrode after cycling. The C 1s spectrum [Figure 4E] revealed five peaks corresponding to C-C, C-H, C-O, C=O, and C-F/C-CO_2. The peaks of C-C and C-H were ascribed to the PVDF adhesives and conductive substances of the electrode, while the C-O, C=O, and C-F/C-CO_2 peaks were mainly related to the decomposition of the electrolyte during the charge/discharge process[37]. The LR-NCM samples showed stronger C-O, C=O, and C-F/C-CO_2 bonds compared to HR-NCM, indicating the suppressed decomposition of the electrolyte and the

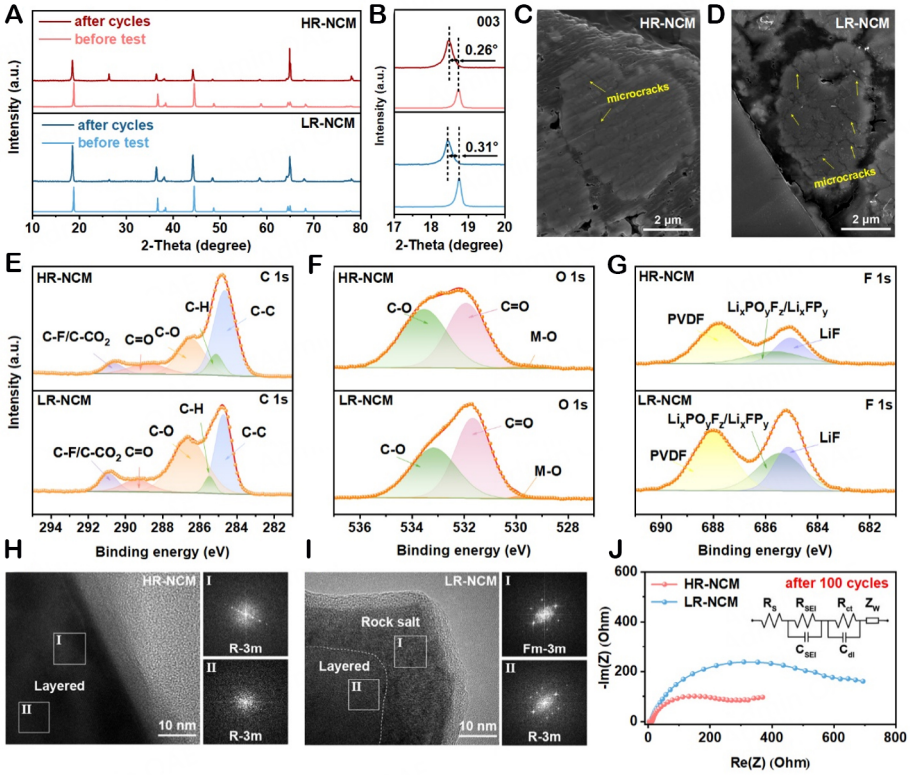

Figure 4. (A) XRD patterns of HR-NCM and LR-NCM cathodes before and after 100 cycles and (B) the magnified patterns of 003 reflections. Cross-section SEM images of cathode electrode after 100 cycles for (C) HR-NCM and (D) LR-NCM. XPS spectra of (E) C 1s, (F) O 1s, and (G) f 1s for HR-NCM and LR-NCM cathodes after 100 cycles at 1 C. TEM and corresponding FFT images after 100 cycles at 1 C for (H) HR-NCM and (I) LR-NCM cathodes. (J) EIS curves measured at 2.7 V (in the discharged state) after 100 cycles for both cathodes.

formation of an additional CEI layer in the cathode with a higher primary particle length/width ratio[38]. Similar results were also observed in the O 1s spectrum [Figure 4F], where the content of C-O/C=O bonds related to the $ROCO_2Li/Li_2CO_3$ was lower in HR-NCM, confirming a decrease in decomposition by-products[39]. In the F 1s spectra [Figure 4G], three types of fluorine derived from PVDF, $Li_xPO_yF_z/Li_xPF_y$, and LiF were identified. The intensities of $Li_xPO_yF_z/Li_xPF_y$ and LiF in the HR-NCM electrode were noticeably lower than those in the LR-NCM electrode, demonstrating suppressed parasitic reactions at the electrode/electrolyte interface[40]. The surface structure of cycled cathodes was further investigated using TEM analysis. As shown in Figure 4H and I, the layered structure (*R*-3*m* space group) of HR-NCM maintains well after cycling, which can be attributed to its excellent morphology integrity that resists electrolyte erosion. In comparison, the surface of cycled LR-NCM exhibits a NiO-like rock-salt phase layer (*Fm*-3*m* space group) with a thickness of ~20 nm due to the aggravated surface parasitic reaction resulting from severe microcracks within the particles.

EIS measurement results of HR-NCM and LR-NCM electrodes before and after 100 cycles are depicted in Supplementary Figure 17 and Figure 4J to reveal the effect of surface phase degradation. The semicircle observed at medium frequencies indicates the charge-transfer process at the electrode/electrolyte interface of the cells[41]. As shown in Supplementary Figure 17, there was no evident difference between the impedance of both cathodes before cycling. However, a much smaller semicircle can be observed for the cycled HR-NCM cathode as compared to the cycled LR-NCM cathode [Figure 4J], implying that the charge transfer resistance (R_{ct}) for the cycled HR-NCM (139 Ω) is significantly lower than that for the cycled LR-

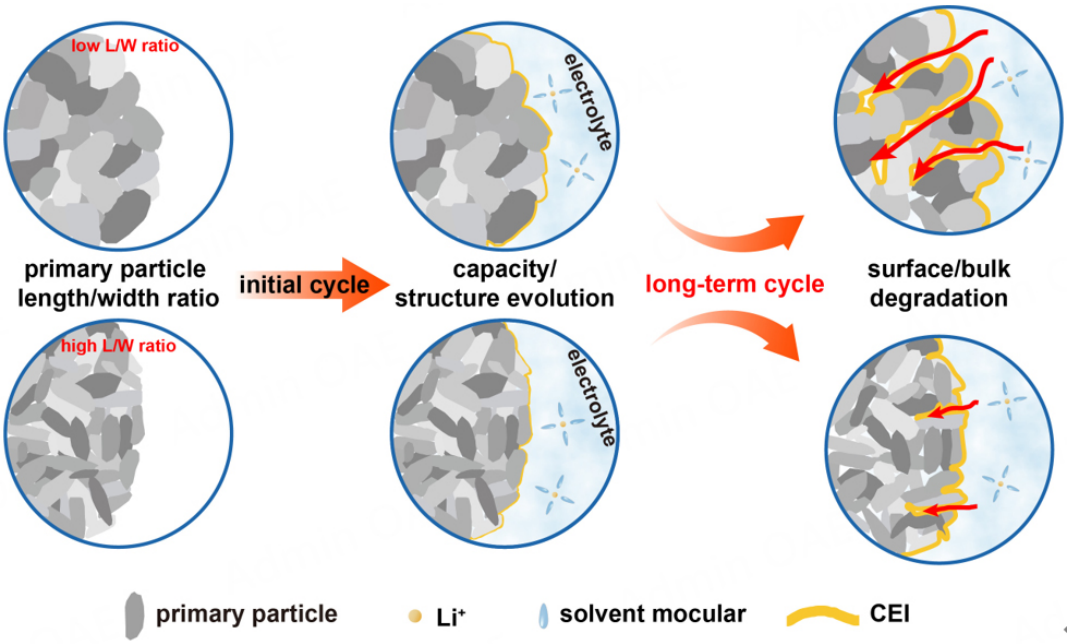

Figure 5. Schematic diagram of the relationship between primary particle length/width ratios and the long-term cycling stability of layered oxide cathode materials.

NCM (320 Ω). The higher R_{ct} of cycled LR-NCM indicated reduced charge transfer kinetics of the cell, which is strongly correlated with the degradation of the surface structure of the cathode. Furthermore, GITT tests were conducted after a certain number of cycles to compare the Li^+ diffusion kinetic property of fatigued cathodes, as shown in Supplementary Figure 18. It is evident that the calculated ion diffusion coefficient during charging processes of both cathode materials decreases upon cycling. This can largely be attributed to the bulk structural deterioration of cathode materials, which severely hinders the ion migration paths. Additionally, the accumulation of NiO-like rock-salt phase formed by the parasitic reaction along the internal interface also further hinders the intercalation/deintercalation of Li ions in Li slabs, damaging the reversible capacity of the materials. However, the HR-NCM cathode consistently exhibits superior ion diffusion abilities than LR-NCM at various states of charge after different cycles, reflecting its structural stability. It is important to note that the Li^+ insertion/extraction would be retarded by higher kinetic barriers, which can lead to incomplete lithiation/delithiation of the cathode material and have a negative effect on the capacity retention of the cathode upon long-term cycling[42].

We explored the relationship between primary particle length/width ratios and the long-term cycling stability of layered oxide cathode materials, as shown in Figure 5. The electrochemical capacity and structural evolution during the initial charge/discharge process of cathodes with various primary particle length/width ratios have no significant difference. However, the regulated microstructure could effectively alleviate the accumulation of microcracks and consequent electrolyte penetration during the prolonged cycling, which results in the surface chemical damage and bulk crystal structure degradation. As a result, the cathode with a higher length/width ratio presented superior capacity retention during long-term cycling.

CONCLUSIONS

In summary, the Ni-rich layered cathode materials with different primary particle length/width ratios were successfully synthesized by adjusting the preparation conditions. The electrochemical capacity and lattice parameter evolution during the initial charge/discharge process were not significantly affected by the

difference of primary particle microstructures in cathode materials. However, the cathode materials with a higher primary particle length/width ratio exhibited superior capacity retention upon long-term cycling. In detail, the regulated primary particle microstructure effectively inhibited the generation and propagation of microcracks in fatigued material particles. Thus, the strengthened mechanical integrity of cathode materials significantly reduced the accumulation of surface chemistry degradation and bulk crystal structural damage during repeat cycling. As a result, the NCM811 material with a higher primary particle length/width ratio maintained considerable Li^+ insertion/extraction reversibility and ion diffusion/transfer kinetics, contributing to excellent reversible discharge specific capacity retention (160 mAh g^{-1} after 200 cycles at 1 C rate). This work highlights the importance of microstructure modulation on the cycling stability promotion of Ni-rich layered oxides to design state-of-the-art high-specific-energy LIB systems.

DECLARATIONS

Acknowledgments

We thank Mr. Chao Li at the Instrument Analysis Center of Xi'an Jiaotong University for conducting Field Emission Transmission Electron Microscope (FE-TEM) analysis and Xiaoqin Wen from Shiyanjia Lab (www.shiyanjia.com) for the CP analysis.

Authors' contributions

Synthesized the materials and electrodes, performed the material characterization and electrochemical tests, and drafted the manuscript: Han D
Executed the SEM measurements: Zhang J, Yang M
Conducted the TEM measurements: Xie K
Carried out the in situ XRD measurements: Peng J, Dolotko O
Provided funding for this work: Huang C, Wu Y, Shao L
Conceptualized and coordinated the activities and facilitated funding for the work: Hua W, Tang W
All authors contributed to revising the manuscript.

Availability of data and materials

The data supporting our findings can be found in the Supplementary Material.

Financial support and sponsorship

The project was supported by the National Key R&D Program of China (2021YFB2400400), the National Natural Science Foundation of China (Grant No. 21905220), the Key Research and Development Plan of Shanxi Province (China, Grant No. 2018ZDXM-GY-135, 2021JLM-36), the National Natural Science Foundation of China (Grant No. 22108218), "Young Talent Support Plan" of Xi'an Jiaotong University (71211201010723), Qinchuangyuan Innovative Talent Project (QCYRCXM-2022-137), the Jiangsu Provincial Department of Science and Technology (BK20201190), "Young Talent Support Plan" of Xi'an Jiaotong University (HG6J003), and "1000-Plan program" of Shaanxi Province.

Conflicts of interest

All authors declared that there are no conflicts of interest.

Ethical approval and consent to participate

Not applicable.

Consent for publication

Not applicable.

REFERENCES

1. Yin S, Deng W, Chen J, et al. Fundamental and solutions of microcrack in Ni-rich layered oxide cathode materials of lithium-ion batteries. *Nano Energy* 2021;83:105854. DOI
2. Zhang X, Liu G, Zhou K, et al. Enhancing cycle life of nickel-rich $LiNi_{0.9}Co_{0.05}Mn_{0.05}O_2$ via a highly fluorinated electrolyte additive - pentafluoropyridine. *Energy Mater* 2021;1:100005. DOI
3. Teichert P, Eshetu GG, Jahnke H, Figgemeier E. Degradation and aging routes of Ni-rich cathode based Li-ion batteries. *Batteries* 2020;6:8. DOI
4. Zhang SS. Problems and their origins of Ni-rich layered oxide cathode materials. *Energy Stor Mater* 2020;24:247-54. DOI
5. Liu L, Li M, Chu L, et al. Layered ternary metal oxides: performance degradation mechanisms as cathodes, and design strategies for high-performance batteries. *Prog Mater Sci* 2020;111:100655. DOI
6. Jung CH, Shim H, Eum D, Hong SH. Challenges and recent progress in $LiNi_xCo_yMn_{1-x-y}O_2$ (NCM) cathodes for lithium ion batteries. *J Korean Ceram Soc* 2021;58:1-27. DOI
7. Kim DH, Song JH, Jung CH, et al. Stepwise dopant selection process for high-Nickel layered oxide cathodes. *Adv Energy Mater* 2022;12:2200136. DOI
8. Kim UH, Park GT, Conlin P, et al. Cation ordered Ni-rich layered cathode for ultra-long battery life. *Energy Environ Sci* 2021;14:1573-83. DOI
9. Heng YL, Gu ZY, Guo JZ, Yang XT, Zhao XX, Wu XL. Research progress on the surface/interface modification of high-voltage lithium oxide cathode materials. *Energy Mater* 2022;2:200017. DOI
10. Yin S, Chen H, Chen J, et al. Chemical-mechanical effects in Ni-rich cathode materials. *Chem Mater* 2022;34:1509-23. DOI
11. Lee SH, Sim SJ, Jin BS, Kim HS. High performance well-developed single crystal $LiN_{i0.91}Co_{0.06}Mn_{0.03}O_2$ cathode via LiCl-NaCl flux method. *Mater Lett* 2020;270:127615. DOI
12. Park GT, Park NY, Noh TC, et al. High-performance Ni-rich $Li[Ni_{0.9-x}Co_{0.1}Al_x]O_2$ cathodes via multi-stage microstructural tailoring from hydroxide precursor to the lithiated oxide. *Energy Environ Sci* 2021;14:5084-95. DOI
13. Huang B, Cheng L, Li X, et al. Layered cathode materials: precursors, synthesis, microstructure, electrochemical properties, and battery performance. *Small* 2022;18:e2107697. DOI
14. Cheng L, Zhou Y, Zhang B, et al. High-rate Ni-rich single-crystal cathodes with highly exposed {0 1 0} active planes through in-situ Zr doping. *Chem Eng J* 2023;452:139336. DOI
15. Namkoong B, Park NY, Park GT, et al. High-energy Ni-rich cathode materials for long-range and long-life electric vehicles. *Adv Energy Mater* 2022;12:2200615. DOI
16. Park GT, Yoon DR, Kim UH, et al. Ultrafine-grained Ni-rich layered cathode for advanced Li-ion batteries. *Energy Environ Sci* 2021;14:6616-26. DOI
17. Kim UH, Park JH, Aishova A, et al. Microstructure engineered Ni-rich layered cathode for electric vehicle batteries. *Adv Energy Mater* 2021;11:2100884. DOI
18. Ren D, Shen Y, Yang Y, et al. Systematic optimization of battery materials: key parameter optimization for the scalable synthesis of uniform, high-energy, and high stability $LiNi_{0.6}Mn_{0.2}Co_{0.2}O_2$ cathode material for lithium-ion batteries. *ACS Appl Mater Interfaces* 2017;9:35811-9. DOI
19. Gan Q, Qin N, Wang Z, et al. Revealing mechanism of Li_3PO_4 coating suppressed surface oxygen release for commercial Ni-rich layered cathodes. *ACS Appl Energy Mater* 2020;3:7445-55. DOI
20. Yoon M, Dong Y, Hwang J, et al. Reactive boride infusion stabilizes Ni-rich cathodes for lithium-ion batteries. *Nat Energy* 2021;6:362-71. DOI
21. Ni L, Chen H, Deng W, et al. Atomical reconstruction and cationic reordering for nickel-rich layered cathodes. *Adv Energy Mater* 2022;12:2103757. DOI
22. Ryu HH, Namkoong B, Kim JH, Belharouak I, Yoon CS, Sun YK. Capacity fading mechanisms in Ni-rich single-crystal NCM cathodes. *ACS Energy Lett* 2021;6:2726-34. DOI
23. Qian R, Liu Y, Cheng T, et al. Enhanced surface chemical and structural stability of Ni-rich cathode materials by synchronous lithium-ion conductor coating for lithium-ion batteries. *ACS Appl Mater Interfaces* 2020;12:13813-23. DOI
24. Ryu HH, Park KJ, Yoon CS, Sun YK. Capacity fading of Ni-rich $Li[Ni_xCo_yMn_{1-x-y}]O_2$ ($0.6 \leq x \leq 0.95$) cathodes for high-energy-density lithium-ion batteries: bulk or surface degradation? *Chem Mater* 2018;30:1155-63. DOI
25. Su Y, Zhang Q, Chen L, et al. Improved stability of layered and porous Nickel-rich cathode materials by relieving the accumulation of inner stress. *ChemSusChem* 2020;13:426-33. DOI
26. Liu H, Xie Z, Qu W, et al. High-voltage induced surface and intragranular structural evolution of Ni-rich layered cathode. *Small* 2022;18:e2200627. DOI
27. Ni L, Guo R, Deng W, et al. Single-crystalline Ni-rich layered cathodes with super-stable cycling. *Chem Eng J* 2022;431:133731. DOI
28. Zhu H, Tang Y, Wiaderek KM, et al. Spontaneous strain buffer enables superior cycling stability in single-crystal Nickel-rich NCM cathode. *Nano Lett* 2021;21:9997-10005. DOI

29. Du B, Mo Y, Li D, Cao B, Chen Y, Zhen H. Relieving the reaction heterogeneity at the subparticle scale in Ni-rich cathode materials with boosted cyclability. *ACS Appl Mater Interfaces* 2022;14:6729-39. DOI
30. Wang L, Wang R, Wang J, Xu R, Wang X, Zhan C. Nanowelding to improve the chemomechanical stability of the Ni-rich layered cathode materials. *ACS Appl Mater Interfaces* 2021;13:8324-36. DOI
31. Nam GW, Park NY, Park KJ, et al. Capacity fading of Ni-rich NCA cathodes: effect of microcracking extent. *ACS Energy Lett* 2019;4:2995-3001. DOI
32. Zhang Y, Zhao C, Guo Z. Simulation of crack behavior of secondary particles in Li-ion battery electrodes during lithiation/de-lithiation cycles. *Int J Mech Sci* 2019;155:178-86. DOI
33. Yang X, Wang S, Han D, et al. Structural origin of suppressed voltage decay in single-crystalline Li-rich layered $Li[Li_{0.2}Ni_{0.2}Mn_{0.6}]O_2$ cathodes. *Small* 2022;18:e2201522. DOI
34. Dai Z, Zhao H, Chen W, et al. In situ construction of gradient oxygen release buffer and interface cation self-accelerator stabilizing high-voltage Ni-rich cathode. *Adv Funct Mater* 2022;32:2206428. DOI
35. Zhuang Y, Zhao Y, Bao Y, Zhang W, Guan M. Research on the electrochemical properties of vanadium boride coated on the surface of NCM811. *J Alloys Compd* 2022;927:166967. DOI
36. Qiu L, Zhang MK, Song Y, et al. Deciphering the degradation discrepancy in Ni-rich cathodes with a diverse proportion of [003] crystallographic textures. *Carbon Energy* 2023;5:e298. DOI
37. Cui Z, Guo Z, Manthiram A. Assessing the intrinsic roles of key dopant elements in high-nickel layered oxide cathodes in lithium-based batteries. *Adv Energy Mater* 2023;13:2203853. DOI
38. Zhou Y, Xiao Z, Han D, et al. Approaching practically accessible and environmentally adaptive sodium metal batteries with high loading cathodes through in situ interlock interface. *Adv Funct Mater* 2022;32:2111314. DOI
39. Zou Y, Meng F, Xiao D, et al. Constructing a stable interfacial phase on single-crystalline Ni-rich cathode via chemical reaction with phosphomolybdic acid. *Nano Energy* 2021;87:106172. DOI
40. Zhou J, Zhang S, Zhou YN, et al. Biomass-derived carbon materials for high-performance supercapacitors: current status and perspective. *Electrochem Energy Rev* 2021;4:219-48. DOI
41. Kim SY, Park CS, Hosseini S, Lampert J, Kim YJ, Nazar LF. Inhibiting oxygen release from Li-rich, Mn-rich layered oxides at the surface with a solution processable oxygen scavenger polymer. *Adv Energy Mater* 2021;11:2100552. DOI
42. Liang JY, Zeng XX, Zhang XD, et al. Mitigating interfacial potential drop of cathode-solid electrolyte via ionic conductor layer to enhance interface dynamics for solid batteries. *J Am Chem Soc* 2018;140:6767-70. DOI